Journal of Materials Chemistry A

PAPER

View Article Online
View Journal | View Issue

Cite this: J. Mater. Chem. A, 2016, 4, 4280

Magnetic catalysts as nanoactuators to achieve simultaneous momentum-transfer and continuous-flow hydrogen production†

Yanyan Liu,[a] Juan Zhang,[a] Xiujun Zhang,[a] Baojun Li,*[a] Xiangyu Wang,[a] Huaqiang Cao,[be] Di Wei,[c] Zhongfu Zhou[d] and Anthony K. Cheetham[e]

Received 29th December 2015
Accepted 18th February 2016

DOI: 10.1039/c5ta10697d

www.rsc.org/MaterialsA

It will be very interesting for many important reactions to endow highly active catalysts with momentum-transfer efficiency. However, the intrinsic magnetism of ferromagnetic catalysts is difficult to exploit due to the interaction between the catalyst and stirring devices. Herein, a catalytically active and super paramagnetic Co–carbon–rGO composite (CCGC) was synthesized and used as a nanoactuator to simultaneously achieve momentum-transfer and hydrolysis of $NaBH_4$ or H_3NBH_3 for hydrogen production. The CCGC magnetically transferred momentum in a batch or continuous flow reactor. The external magnetic field can drive the catalyst to transfer momentum for excellent agitation. The catalyst can be fixed at an appointed position in the continuous flow for efficient separation. The separation of the catalyst from the reaction mixture also becomes facile. The CCGC showed superior retention as a pollutant adsorbent for the removal of Rhodamine B (Rh-B) from water in the absence of magnetic or mechanical stirring apparatus. The unique momentum-transfer properties, as well as excellent catalysis and adsorption, warrant its promising application in the corresponding fields.

1. Introduction

In recent years, research on magnetic nanoparticles (NPs) has received considerable attention for its benefits in addressing energy and environmental problems.[1] Magnetic NPs can be easily separated from a medium by using an external magnetic field. The replacement of precious metal catalysts by cheap and abundant metals is a major goal of sustainable chemistry, and magnetic cobalt NPs are becoming good candidates for catalytic applications.[2] For example, Co NPs can be used as catalysts for the hydrolysis of sodium borohydride ($NaBH_4$) and ammonia borane (H_3NBH_3) to produce high purity hydrogen.[3–5]

Dispersed Co NPs readily agglomerate and oxidize when exposed to air, which may result in the formation of an anti-ferromagnetic CoO phase and a decrease in catalytic activity. To solve this problem, significant progress in material design has been made through a wrapping strategy to fabricate core–shell structures. Co NPs can be protected as cores by being wrapped in shells composed of porous polymers,[6–10] zeolites,[11–13] carbon,[14–17] and so on. The core–shell structure is beneficial to the stability of the metal NPs in composite materials.[18–20] Carbon shells exhibit unique advantages due to their chemical inertness and structural stability, and the shells also facilitate the creation of a porous structure in the material synthesis process.

In a heterogeneous catalytic reaction, the rate is often controlled by the diffusion of the reactants between the liquid reaction phase and the solid catalyst. The reaction medium must therefore be stirred vigorously in order to bring adequate catalytic activity into play. Typically, mechanical or magnetic stirring will result in magnetic catalysts being adsorbed on the stirring device, which will decrease the catalytic activity. The intrinsic ferromagnetism of Co NPs can respond to an external magnetic field, so while changing or moving the field, nano-structures containing Co NPs may transfer momentum to the fluid medium. In a catalytic reaction system, therefore, Co NPs or Co NPs@carbon core–shells can play a dual role as both a catalyst and as stirring bars or rods. Thus, additional magnetic stirring devices will not be needed in the reaction system, while substantial efficiency can still be obtained from the catalytic magnetic Co NPs or Co NPs@carbon core–shells, which will maintain a homogenous reaction system.

The main challenge is that small Co NPs cannot transfer momentum efficiently because of the weak interaction between the Co NPs and the fluid medium over long distances, leading to low momentum transfer and a poor mixing effect. However, if

[a]College of Chemistry and Molecular Engineering, Zhengzhou University, Zhengzhou 450001, P R China. E-mail: lbjfcl@zzu.edu.cn
[b]Department of Chemistry, Tsinghua University, Beijing 100084, P R China
[c]Nokia R&D UK, Broers Building, 21 JJ Thompson Avenue, Cambridge, CB3 0FA, UK
[d]Shanghai Key Laboratory of Modern Metallurgy and Materials Processing, Shanghai University, Shanghai 200072, P R China
[e]Department of Materials Science & Metallurgy, University of Cambridge, 27 Charles Babbage Road, Cambridge CB3 0FS, UK

† Electronic supplementary information (ESI) available: Experimental details and some characterization results. See DOI: 10.1039/c5ta10697d

Co NPs can be assembled onto a larger scale support, such as graphene nanosheets, this will enhance the interaction between the catalyst and reaction medium; we can stir the fluid medium efficiently while enhancing the momentum transfer (Fig. 1).

Due to their large surface area, light weight and corrosion resistance, graphene and reduced graphene oxide (rGO) sheets on the micro scale are perfect substrates to support catalytically active metal NPs or core–shell structures as catalyst or adsorption separation materials.[21,22] It is generally difficult to maintain the large surface area of micro scale graphene and rGO due to the strong van der Waals interaction between them.[23] However, the presence of inorganic NPs anchored on graphene or rGO sheet surfaces can prevent them from aggregating while effectively retaining their surface area. We therefore anchored Co NP@carbon core–shells onto the surface of rGO nanosheets in order to fabricate three dimensional Co–carbon–rGO composites (CCGCs). The CCGCs possess large surface areas and can be used as adsorbents for water purification and other environmental applications.[24–26] The super paramagnetic CCGCs can be agitated under a moving or changing magnetic field. At the same time, the plate-like structure of the CCGCs on the micrometer scale can effectively transfer momentum to the reaction system, thereby avoiding the need for metal stirring apparatus. In the case of adsorption, momentum self-transfer and separation based on the magnetic response is still displayed by the functional CCGC materials. The separation of nanocatalysts from continuous flow reaction mixtures is another problem for industrial processes. Generally, some highly fine filtration membranes are necessary, which often cause a large pressure drop. The unique super paramagnetism of Co NPs can be used to fix nanocatalysts at an appointed position and separate nanocatalysts from continuous flow reaction mixtures by an external magnetic field.

In this paper, we report a combined hydrothermal and calcination process to fabricate the CCGC nanocomposites. The Co NP@carbon core–shell structure improved the stability of the Co NPs in the CCGC. The 3D composite structure endowed the CCGC with enhanced adsorption capacity and separation efficiency. The intrinsic super paramagnetism enabled the CCGC to perform momentum self-transfer, magnetic fixation and separation in a practical process. Excellent catalytic activities were obtained in the batch and slurry-bed reactor at room temperature in the absence of a magnetic stirring bar or rod. The CCGC also exhibited fast adsorption rates and higher adsorption efficiency.

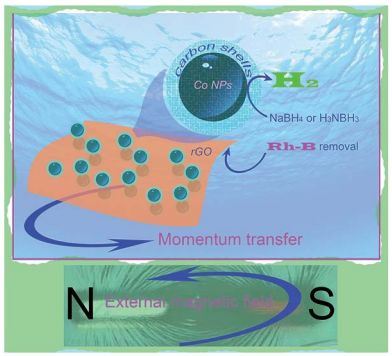

Fig. 1 The momentum-transfer mechanism of the CCGC.

2. Experimental section

Material synthesis

Graphite oxide was prepared from natural graphite according to a modified Hummers method.[27] First, an aqueous solution (200 mL) of graphite oxide (200 mg) was stirred and ultrasonicated for 2 h to form an aqueous suspension of graphene oxide (GO). An aqueous solution (20 mL) of Co nitrate (13.982 g) and an aqueous solution (15 mL) of polyvinyl pyrrolidone (PVP, MW: 58 000, 150 mg) were added to the aqueous suspension of GO under stirring and then the mixture was stirred for a further 4 h. Then an aqueous solution (20 mL) of sodium hydroxide (3.844 g) was added into the mixture followed by further stirring for 0.5 h. An aqueous solution of glucose (4.504 g) was then added and the mixture was stirred for another 0.5 h. The mixture was transferred into a Teflon-lined stainless steel autoclave (500 mL) and heated to 180 °C for 24 h. After cooling to room temperature naturally, the resulting solid was washed with water and dried at 80 °C in air for 12 h. After being heated to 550 °C with a heating rate of 10 °C min^{-1} and kept for 1 h under N_2 flow, the solid powder was cooled and added into an ethanol solution (15 mL) (*Caution! The sample readily combusts when exposed to air*). After magnetic separation and drying for 30 min at 80 °C, the CCGC-I sample was obtained as a black powder. With various amounts of glucose, CCGC-II (4.003 g of glucose) and CCGC-III (3.603 g of glucose) were also prepared by the same method. Through a similar process to that of CCGC-I, a Co–C composite was obtained with glucose (4.504 g) in the absence of rGO. The elemental Co contents in CCGC-I, CCGC-II, CCGC-III and Co–C were calculated from TG curves to be 75%, 81%, 82% and 78%, respectively (Fig. S1, see ESI†). Two Ru-doped CCGC catalysts (CRGC-I: 1 mol% of Ru, and CRGC-II: 2 mol% of Ru) were synthesized through a similar route to that of CCGC with the addition of $RuCl_3 \cdot xH_2O$ as the Ru source (Experimental details, see ESI†). All composites were ground in an agate mortar for 3 min before being used as catalysts and adsorbents.

Characterization

The phase structure of the as-prepared product was characterized by X-ray powder diffraction (XRD, Bruker D8 advance with Cu K_α $\lambda = 1.5418$ Å). The average crystallite size of the Co NPs was estimated using the Scherrer formula: $D_h = \lambda/(\beta_h \cos \theta_h)$, where D_h is the domain size of the diffraction line, λ is the wavelength of the Cu K_α source used, β_h is the width in radians of the diffraction peak measured at half-maximum intensity (fwhm) corrected for instrumental broadening, and θ_h is the angle of the particular (*hkl*) reflection. Raman spectra were recorded on a Renishaw RM-1000 with excitation from the 514 nm line of an Ar-ion laser with a power of about 5 mW. The morphology of the as-prepared product was studied using transmission electron microscopy (TEM, JEOL, JEM-2010F electron microscope, operating at 200 kV). Magnetic hysteresis

loops were measured on a Physical Property Measurement System (PPMS-9T) at 300 K with an applied magnetic field (H_{max} = 40 kOe). The magnetization data were acquired in both field cooled (FC) and zero-field cooled (ZFC) modes; the sample was first cooled to low temperatures in an applied field (100 Oe) or in the absence of such a field, and the magnetization data were recorded under an applied field of 100 Oe upon heating.

Hydrogen generation in batch reactor

Hydrogen generation was studied with the typical water displacement method.[20] The catalyst (20 mg) and $NaBH_4$ (80 mg) or H_3NBH_3 (80 mg) were placed in a three-neck round-bottom glass flask and then deionized water (20 mL) was added. The flask was placed on a magnetic stirrer. In magneton-stirring mode, a magneton was employed in the flask. In self-stirring mode, only the catalyst and reaction mixture were loaded in the flask. The stirring rate was fixed at 500 rpm and other stirring rates were used only if noted. An inverted and water-filled gas burette in a water-filled vessel was used to monitor the volume of the evolved H_2. The hydrogen generation specific rates per gram of catalyst (r_B) were calculated using the information in the initiating and stabilizing stages (140 mL of hydrogen generated) according to the following formula:

$$r_B = \frac{140\ (\mathrm{mL})}{t_{140}\ (\mathrm{min}) \times w_c\ (\mathrm{g})} \quad (1)$$

Here, r_B is denoted the hydrogen generation specific rate, t_{140} represents the time taken for 140 mL of hydrogen generation, and w_c is the weight of the catalyst.

Hydrogen generation in slurry-bed reactor

The catalyst (20 mg) and water (80 mL) were placed into a glass slurry-bed reactor (100 mL) fixed onto a magnetic stirrer. An aqueous solution of $NaBH_4$ (0.1 M or 0.2 M, 60 mL) was added into the reactor bottom through an entrance at a flow rate of 1.30 mL min^{-1} by an injector pump. The liquid reaction mixture exited from the reactor top through an export tube. The retention time of the reaction liquid in the reactor was controlled at 61.5 min. A stable continuous flow state was kept for 46 min. The stirring rate of the magnetic stirrer was fixed at 500 rpm. The hydrogen left the reactor through a top tube. The hydrogen volume was measured in the same inverted and water-filled gas burette in a water-filled vessel.

Dye adsorption

Rhodamine B (Rh-B) was used as a probe molecule to evaluate the adsorption performances of the CCGCs. The characteristic optical absorption peak of Rh-B at 544 nm was chosen to monitor the adsorption process. The experiments were carried out according to the following procedure: dried powder CCGC (50 mg) was dispersed in an aqueous solution (1.0×10^{-5} M, 100 mL) of Rh-B under a constant stirring of 500 rpm for 0.5 h. At given intervals, the suspension (4 mL) was extracted and then centrifuged at 4000 rpm for 1 min to separate the adsorbent from the supernatant. A visible spectrophotometer (721, Shanghai Qinghua Tech. Ins. Lim.) was used to measure the spectra.

3. Results and discussion

The designed structure was constructed by synthesizing core–shells and anchoring them onto the surface of rGO nanosheets in a hydrothermal and carbothermal reduction process, as described above (Scheme S1†). Firstly, in the deposition–precipitation process, $Co(OH)_2$ NPs were obtained from a Co precursor and deposited onto the surface of GO in a suspension of GO. In the subsequent hydrothermal treatment, some poly-sugar shells were wrapped on the $Co(OH)_2$ NPs to form core–shell structures. Finally, a carbothermal reduction was performed under a nitrogen atmosphere to transform the $Co(OH)_2$ NPs to Co NPs and the poly-sugar shells to carbon shells, respectively. The GO sheets were also reduced to rGO sheets by the poly-sugar shells during heat treatment.[28] After these processing steps, CCGC-n (n = I to III) and Co–C were successfully fabricated.

The nanoscale morphology and microstructure of the CCGCs were monitored by TEM and HRTEM (Fig. 2 and S2, see ESI†). The rGO nanosheets were coated with the Co NPs@carbon core–shells (Fig. S2, see ESI†). The morphologies of the CCGCs are almost the same as the rGO sheets in the micrometer range. The Co NPs@carbon core–shells are mainly anchored onto the rGO surface or intercalated between the rGO nanosheets. No Co NPs@carbon core–shell structures without rGO nanosheets were observed for CCGC. The Co NPs@carbon core–shells exhibit a wide diameter distribution in the nanoscale range (Fig. S2, see ESI†). Without the rGO template, Co–C clearly shows a typical Co–carbon submicrometer sphere with a diameter of *ca.* 200–300 nm (Fig. S2g and h, see ESI†). Some aggregation of Co–C can also be observed because of the uncontrollable growth of the carbon shells. The core–shells are composed of Co NPs with diameters ranging from 20 to 40 nm and carbon shells with thicknesses of 10–20 nm (Fig. 2a and b, see ESI†). A porous structure can be observed in the carbon shells (Fig. 2b and c). Due to the overlap of the porous carbon shells, the 3D lattice fringes of the face-centred cubic Co NPs

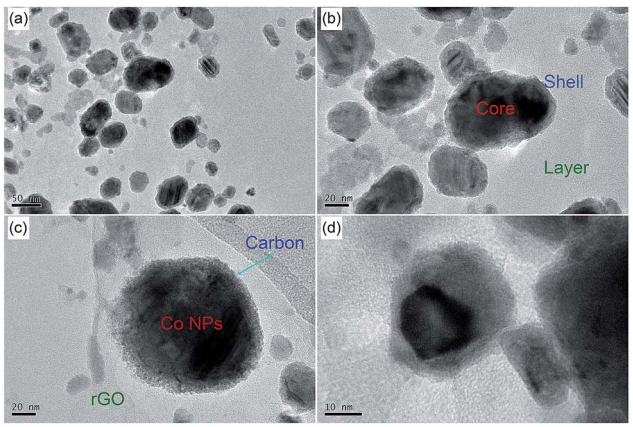

Fig. 2 (a–d) TEM images of CCGC-I.

formed on the rGO nanosheets cannot be observed clearly in the HRTEM images (Fig. 2c and d). The lattice fringes with a spacing of 0.176 nm may correspond to the (200) plane of the face-centred cubic Co, which is consistent with the (200) diffraction peak in the XRD pattern.[29]

From the XRD patterns of CCGC (Fig. 3a), the presence of three main peaks 44.2° (111), 51.5° (200) and 75.9° (220) matches the cubic β-phase of Co with lattice parameters of a = 3.544 Å (JCPDS card no. 89-4307), which confirms the existence of Co metal on the CCGC nano-composites.[30] The absence of a peak at 11.3° shows that the reduction of GO to rGO was almost complete. The wide weak peak ranging from 26.8° to 38.0° indicates that graphene was highly dispersed in CCGC.[31] Calculations using the Scherrer equation and the (111) plane in the XRD patterns of the CCGCs reveal that the crystallite sizes of the Co NPs in CCGC-I, CCGC-II, CCGC-III and Co–C are 44.8, 51.1, 54.4 and 37.5 nm, respectively.[32] In the Raman spectra of CCGC-I (Fig. 3b), the peaks at 1599 and 1354 cm^{-1} can be attributed to the G and D bands, respectively, of the graphene domains in the carbon components.[33] The G band corresponds to the in-plane vibration of sp^2 carbon atoms in a 3D hexagonal lattice, whereas the D band corresponds to the vibrations of sp^3 carbon atoms of disordered graphite.[34] The typical characteristic for the reduction of GO is that the G band shifts to a lower number. A value of I_D/I_G (0.72 : 1) was calculated for CCGC-I (Fig. 3b), compared with the value of I_D/I_G for GO (0.83 : 1). The variation in the value of I_D/I_G confirms that the reduction of GO resulted in small graphene nanosheets and that a large proportion of sp^2 carbon atoms are present in the structures.[27] The conclusions from the Raman spectra and FT-IR spectra analysis are in accord with the above XRD results.

The surface composition of the CCGC-I nanocomposites was determined by XPS measurements. In the XPS spectra, the main peaks observed in the survey scans of CCGC-I were the C 1s, O 1s, and Co 2p peaks centered at *ca.* 285, 530, and 778–800 eV, respectively (Fig. S4, see ESI†). The fine spectra of C 1s for CCGC-I could be ascribed to C with various oxygen functionalities, namely, C=C (sp^2 carbon, C1), C–O (sp^3 carbon, C2), and C=O (sp^3 carbon, C3) bonds, with binding energies of about 284.7, 286.2, and 288.8 eV, respectively.[35] Fig. S4c† shows the main peak at 778.5 eV for CCGC-I, which can be attributed to metallic Co and reveals that zero-valent Co is obtained after reduction from Co(II).[36] The peaks at 780.6 and 796.5 eV (the satellite peak) can be assigned to Co(II) species at the surface of CCGC-I. This result implies the possible coexistence of metallic Co and Co^{2+} in the surface region of CCGC-I.[37]

The specific surface areas and pore volume of CCGC-I were measured to be about 85 $m^2\ g^{-1}$ and 0.13 $cm^3\ g^{-1}$, respectively (Fig. S5a, see ESI†). Such a large specific surface area is important for enhancing catalytic activity. These textural properties are comparable to those of typical catalysts and adsorbent materials. The pore size distributions are narrow in the range from 10 to 30 nm with a peak pore diameter of 19.2 nm (Fig. S5b, see ESI†). The mesoporosity may be due to the intercalation structure of rGO with the Co NPs@carbon core–shells.[38]

The magnetization curves of CCGC-I were measured at 300 K in a variable applied field (Fig. 3c). The hysteresis loop of CCGC-I at 300 K showed that a very small coercivity (H_c) of 208 Oe is required to degauss CCGC-I (inset ii in Fig. 3c). The very low remanence magnetization (M_r) of 8.7 emu g^{-1} is also consistent with the small H_c. A small squareness ($S_r = M_r/H_c$) of 0.041 was obtained for CCGC-I. These parameters are evidence for the super paramagnetic character of CCGC-I.[39] The super paramagnetism and strong magnetic response ensure that CCGC-I can be separated from the liquid phase mixture system. The temperature dependence of magnetization in the temperature range of 5 K to 300 K was measured under an applied field of 100 Oe following the zero field cool (ZFC) and field cool (FC) protocols (Fig. 3d). The FC magnetization curve exhibits a monotonous decreasing trend. The ZFC magnetization curve shows a peak at 246.6 K, which is the Curie temperature (T_C).[40] Above the Curie temperature, the ferromagnetic CCGC-I gradually transforms to a paramagnetic material. In the temperature range from 5 K to 300 K, high magnetization (12.25–13.17 emu g^{-1}) was obtained throughout in the two modes. At 300 K, a high magnetization of 12.7 emu g^{-1} still remained. The high and stable magnetization ensures that CCGC-I is readily magnetized by an applied field in a wide temperature range.[41] The superior magnetic properties of CCGC-I provide a potential application in the momentum-transfer process (inset iii in Fig. 3c). Accordingly, when CCGC-I is dispersed into a reaction mixture or solution and magnetized by a moving or changing external field, momentum will be transferred from the external field to the Co NPs in CCGC-I. The robust anchoring of the Co NP cores helps CCGC-I to transfer momentum to the rGO nanosheets and then to the solution. The stirring momentum-transfer can be replaced by this self-momentum transfer mode. This momentum-transfer mode was investigated while following catalytic reactions and adsorption separations.

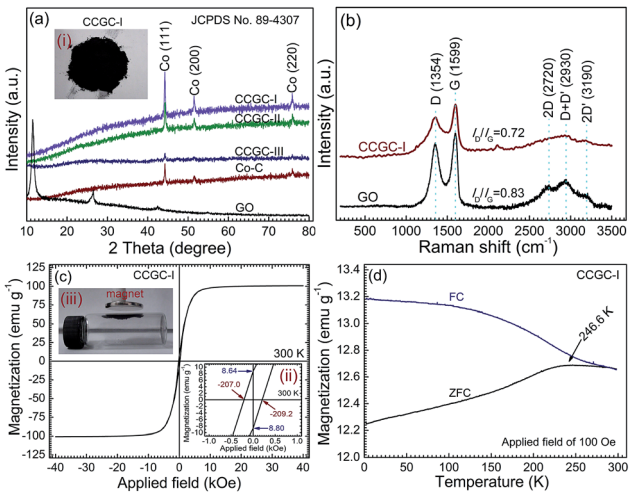

Fig. 3 (a) XRD patterns Co–C, CCGC, and GO, (b) Raman spectra of CCGC-I and GO, (c) hysteresis loop at 300 K of CCGC-I, (d) zero field cooling and field cooling magnetization curves with an applied field of 100 Oe. Inset (i) in (a) is the photograph of CCGC-I, inset (ii) in (c) is an enlarged view of the hysteresis loop of the CCGC-I and inset (iii) in (c) is the photograph of the CCGC-I response to a magnet.

The catalytic performance and momentum-transfer properties of the CCGCs for hydrogen generation from the hydrolysis of $NaBH_4$ and H_3NBH_3 were investigated in a batch reactor (Fig. 4a and b and S6a, see ESI†). When a magneton was used to stir the reaction system, serious attraction of CCGC was observed (Fig. S6c, see ESI†). Because of the bad distribution of catalyst in the reaction mixture, the catalytic performances were influenced negatively. Various stirring rates exhibit clear positive effects on the hydrogen generation specific rates (Fig. S7a, see ESI†). In various concentrations of aqueous solutions of $NaBH_4$, CCGC provided different r_B (Fig. S7b, see ESI†). In solutions of 0.2 and 0.3 mol L^{-1}, CCGC provided the highest r_B (Fig. S7b, see ESI†).

In contrast to that in magneton stirring mode, CCGC-I possesses the highest r_B of 767 mL min^{-1} g^{-1} at room temperature in self-stirring mode (Fig. 4b). The conversion rate of the hydrolysis of $NaBH_4$ reached 97% in 16 min, indicating that CCGC-I possesses high catalytic activity for hydrogen production. The excellent catalytic performance of CCGC-I can be attributed to the relatively high dispersion of Co NPs and the existence of pores in the carbon shells.[42] In the absence of a stirring bar, three CCGC catalysts have higher catalytic rates in self-stirring than magneton-stirring modes (Fig. 4b and S7, see ESI†). In self-stirring mode, the stirring rates exhibited no clear influence on the hydrogen generation specific rates and the substrate concentrations exhibited similar effects on hydrogen generation specific rates to those in magneton-stirring mode (Fig. S7, see ESI†). Momentum-transfer from the changing external magnetic field to the reaction mixture was performed effectively by the CCGCs themselves. In a controlled blank experiment, very slow hydrogen production rates can be obtained without a catalyst (Fig. S8c, see ESI†). In comparison, Co–C exhibits a lower catalytic activity (Fig. S8c, see ESI†). The reason for the sluggish catalytic rate on Co–C can be mainly attributed to the diminished specific surface area of Co–C without rGO. The intrinsic magnetism of the Co NPs leads to decreased dispersion of the catalyst in the presence of a magnetic stirring bar, due to serious catalyst adsorption on the bars. It also clearly shows that the catalytic rate is higher with self-stirring than with a stirring bar. The catalytic reaction at different temperatures was investigated (Fig. 4c). The reaction shows zero-order kinetics in the temperature range from 303 K to 328 K. An Arrhenius plot of ln *k versus* the reciprocal absolute temperature ($1/T$) was obtained as a straight line (Fig. 4d). The apparent activation energy (E_a) of the catalytic reaction was calculated according the following Arrhenius eqn (2).

$$k_0 = A \exp\left(-\frac{E_a}{RT}\right) \quad (2)$$

Here k_0 denotes the rate constant, R is the ideal gas constant, A represents the pre-exponential factor, and T is the reaction temperature. The Arrhenius activation energy of CCGC-I was determined to be approximately 47.11 kJ mol^{-1} from the slope of the Arrhenius plot. This E_a value is lower compared to those reported for other catalytic materials.[43,44] The conversion rate of H_3NBH_3 hydrolysis was over 90% in 17.5 min (Fig. 4e).

In order to improve the catalytic activity of CCGC, two Ru-doped CCGC catalysts (Ru : Co molar ratio of 1 : 99 and 2 : 98 for CRGC-I and CRGC-II) were synthesized through a similar route to that of CCGC-I with the addition of $RuCl_3$ as a Ru source (Fig. S9–11, see ESI†). CRGC was evaluated as a catalyst for the hydrolysis of $NaBH_4$ in a batch reactor. Higher catalytic activities with larger r_B than those of CCGC were obtained, with CRGC (Fig. 4f). The r_B values of 1378 and 1716 mL min^{-1} g^{-1} were calculated for CRGC-I and CRGC-II, respectively. These positive changes illustrate the potential development of CRGC catalysts for more high performance industrial catalysts through surface adjustment.

In the heterogeneous catalysis industry, continuous flow processes are often preferred due to their high efficiency, lower operation costs, excellent stability and safety, compared to batch processes. For nanocatalysts used in a liquid phase reaction, the slurry-bed reactor is a suitable option because of the good dispersion state. The only main problem is the effective separation of the catalyst from the reaction mixture. A high fine filtration membrane and tedious technology are required generally. It is still a challenge to effectively use nanocatalysts in a continuous flow process. The magnetic property of the Co NPs in CCGC provides a nice opportunity for effective separation. A slurry-bed reactor was designed and used for the continuous hydrolysis of $NaBH_4$ (Fig. 5a and S6b, see ESI†). The main

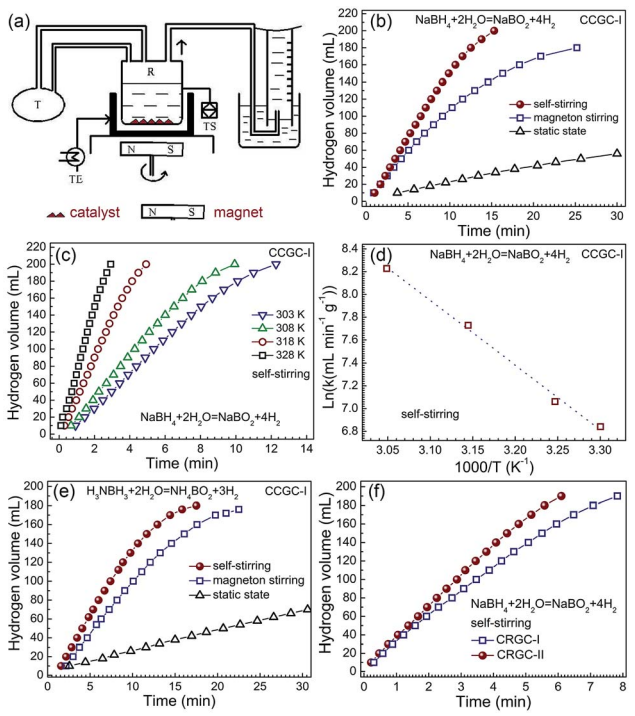

Fig. 4 (a) A simplified diagram of the batch reactor. Abbreviations: R, reactor; P, pump; T, tank; TE, thermo element; TS, thermo sensor. The catalytic performances of CCGC-I in hydrogen generation (b) from $NaBH_4$ under various stirring modes at room temperature, (c) under self-stirring mode at various temperatures, (d) corresponding plot of ln *k versus* $1/T$, (e) from H_3NBH_3 under various stirring modes at 303 K, and the catalytic performances of (f) the CRGC in hydrogen generation from $NaBH_4$ at 303 K.

feature is that an external magnetic field was employed to fix and drive the catalysts in the reactor. Due to the strong interaction between the catalyst and magnetic field, the catalyst cannot leave the reactor with the liquid flow. This slurry-bed reactor provided a stable and effective continuous flow process for hydrogen generation from $NaBH_4$ (Fig. 5b–d). In the initiating stage (first 11 min), the stable continuous flow is forming, so r_B reaches up to 1018 mL min^{-1} g^{-1} with the solution of $NaBH_4$ (0.2 M). In the following stabilizing stage (second 35 min), a constant r_B of 714 mL min^{-1} g^{-1} was maintained. In the ending stage (last 20 min), the lowest r_B of 503 mL min^{-1} g^{-1} was obtained because the continuous flow state stopped (Fig. 5c). The continuous flow process is also reliable for $NaBH_4$ solutions of other concentrations (Fig. 5d). It is noteworthy that this slurry-bed process can be stopped at any time by the external magnetic field, which can help the catalyst to separate from the reaction mixture (Fig. S6d, see ESI†). The stable hydrogen generation specific rate in the stabilizing stage is comparable to that in the batch reactor (767 mL min^{-1} g^{-1}). The CCGC catalysts are suitable for continuous flow processes because of their super paramagnetism.

There is still a question regarding the magnetic properties of the CCGC and CRGC catalysts and the external magnetic field. Many substrates and products possess diamagnetism. They exhibit a very weak repulsion force because of their very low (10^{-5}) negative magnetic susceptibility (χ). Some paramagnetic molecules will show a very weak attractive force because of their very low (10^{-5}) positive magnetic susceptibility. Super paramagnetic materials generally possess very high (10^{3}) positive magnetic susceptibility. An external magnetic field is enough to drive and fix the catalysts. Compared to the high magnetic susceptibility of the catalysts, the magnetic susceptibility of the substrates and products can be ignored. Namely, the external magnetic field and magnetism of the catalysts are not enough to affect the catalysis process. Even though, in a very strong external magnetic field, the catalytic activity of magnetic NPs can be influenced positively.[45–47]

CCGC-I was also used as an adsorbent to remove Rh-B from aqueous solution (Fig. 6). The CCGCs showed much higher Rh-B (1.0×10^{-5} M) adsorption capacity than those of Co–C and rGO (Fig. 6a). When added to CCGC-I, the Rh-B concentration rapidly decreased (Fig. 6a). A maximum adsorption amount of 9.6 μg mg^{-1} was measured for CCGC-I, and CCGC-I had a higher Rh-B adsorption ratio with self-stirring than in the static mode (Fig. 6b). In comparison, CCGC-I exhibits a similar adsorption rate with self-stirring to that with magneton-stirring. The Co NPs played a key role in the self momentum-transfer performance. The $\ln(C_0/C)$ plot shows a linear relationship with adsorption time, which reveals that the adsorption of dye molecules proceeds through a pseudo-first-order kinetic reaction (Fig. 6c).[48,49]

A magnet was used to separate CCGC-I from ethanol media. Using recycled CCGC-I to remove Rh–B from water, completed adsorption was achieved within 2 min. After recycling for the 8th time, complete adsorption was achieved within 3 min (Fig. 6d). CCGC-I shows superior retention as a pollutant adsorbent for the removal of Rh-B from water. When CCGC-I without removal of the Rh-B was directly immersed into another aqueous solution (20 mL) of Rh-B (1.0×10^{-5} M), the same absorption process was still efficiently executed. The absorbent rate is retained through successive adsorption cycles and the removal of Rh-B from water was also completed within 5 min (Fig. 6d). After more than three cycles, the maximum adsorption amount of CCGC-I was still sustained at 9.6 μg mg^{-1}, which is comparable to that reported in the literature.[5,10,11,49] The adsorption capacity and excellent momentum-transfer performances of CCGC-I are clearly due to the existence of the Co NPs@carbon core–shell structure on the rGO nanosheets.

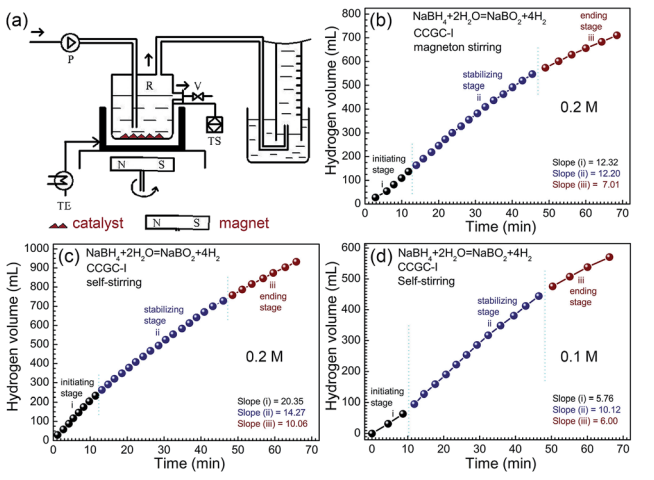

Fig. 5 (a) A simplified diagram of the slurry-bed reactor. Abbreviations: R, reactor; P, pump; T, tank; TE, thermo element; TS, thermo sensor; V, valve. The catalytic performances of CCGC-I in hydrogen generation from $NaBH_4$ in the continuous flow slurry-bed reactor under (b) magneton-stirring and (c, d) self-stirring modes at 303 K.

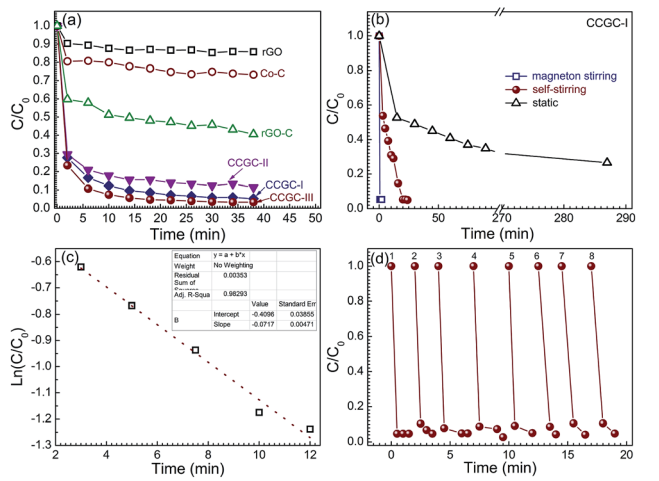

Fig. 6 (a) C/C_0 *versus* time plots for adsorption of Rh-B solution (100 mL) with various absorbents (50 mg) under magnetic stirring at 500 rpm, (b) C/C_0 *versus* time plots for adsorption of Rh-B solution (150 mL) with recycling of CCGC-I (50 mg) under various stirring modes, (c) $\ln(C/C_0)$ *versus* time plots for adsorption of Rh-B solution (220 mL) with CCGC-I (50 mg), and (d) C/C_0 *versus* time plots for adsorption of Rh-B solution (20 mL) with recovered CCGC-I (40 mg).

4. Conclusions

In conclusion, a core–shell@nanosheet composite, CCGC, can be synthesized by a facile hydrothermal treatment followed by calcination. The core–shells, namely, Co NPs capsulated into porous carbon shells, were anchored homogeneously onto the surface of rGO. Co NPs endowed the CCGCs with catalytic activity and super paramagnetic properties. The CCGC was used as a catalyst to achieve the hydrolysis of $NaBH_4$ or H_3NBH_3 for hydrogen production in batch or slurry-bed reactors. In both reactors, the aim of efficient magnetic momentum transfer was reached by the CCGC as a nanoactuator with high hydrogen generation rates. The role of a stirring bar or rod were subsumed by the moving external magnetic field. In the slurry-bed reactor, the CCGC catalysts were derived and fixed at an appointed position to prevent them from leaching from the reactor. The efficient separation replaced a high fine filtration membrane. The CCGCs also showed superior retention as a pollutant adsorbent for the removal of Rh-B from water. A higher adsorption efficiency and faster adsorption rate were obtained on the CCGCs in the absence of a magnetic stirring rod. The excellent catalysis and adsorption removal, as well as momentum self-transfer properties, point to promising applications in water purification and other corresponding fields. It is important for the synthesis of rGO-based composite functional materials to anchor the core–shell structures on nanosheets. A composite functionalized with magnetic NPs can be guided, controlled, separated and collected by applying an external magnetic field. This research opens a new avenue in chemical engineering and biomedical applications.

Acknowledgements

Financial support from the National Natural Science Foundation of China (21401168) is acknowledged. Prof. Huaqiang Cao thanks the 973 Program (2013CB933804) for financial support. Financial supports from the NSFC-Henan Joint Foundation (U1204203) and the Outstanding Young Teacher Development Fund of Zhengzhou University (1421316037) are acknowledged.

Notes and references

1 A. Lv, C. Hu, Y. Nie and J. Qu, *Appl. Catal., B*, 2012, **117–118**, 246–252.
2 U. B. Demirci and P. Miele, *Phys. Chem. Chem. Phys.*, 2014, **16**, 6872–6885.
3 M. Rakap, E. E. Kalu and S. Özkar, *Int. J. Hydrogen Energy*, 2011, **36**, 254–261.
4 J. Z. Zhao, H. Ma and J. Cheng, *Int. J. Hydrogen Energy*, 2007, **32**, 4711–4716.
5 K. Aranishi, H. L. Jiang, T. Akita, M. Haruta and Q. Xu, *Nano Res.*, 2011, **4**, 1233–1241.
6 Y. Liu, W. M. Xuan and Y. Cui, *Adv. Mater.*, 2010, **22**, 4112–4135.
7 T. Wen, X. L. Wu, X. L. Tan, X. K. Wang and A. W. Xu, *ACS Appl. Mater. Interfaces*, 2013, **5**, 3304–3311.
8 C. L. Zhang, L. Wu, D. Q. Cai, C. Y. Zhang, N. Wang, J. Zhang and Z. Y. Wu, *ACS Appl. Mater. Interfaces*, 2013, **5**, 4783–4790.
9 L. Zadoina, K. Soulantica, S. Ferrere, B. Lonetti, M. Respaud, A. F. Mingotaud, A. Falqui, A. Genovese, B. Chaudret and M. Mauzac, *J. Mater. Chem.*, 2011, **21**, 6988–6994.
10 H. B. Li, X. C. Gui, L. H. Zhang, S. S. Wang, C. Y. Ji, J. Q. Wei, K. L. Wang, H. W. Zhu, D. H. Wu and A. Y. Cao, *Chem. Commun.*, 2010, **46**, 7966–7968.
11 B. J. Li and H. Q. Cao, *J. Mater. Chem.*, 2011, **21**, 3346–3349.
12 Y. B. Sun, D. D. Shao, C. L. Chen, S. B. Yang and X. K. Wang, *Environ. Sci. Technol.*, 2013, **47**, 9904–9910.
13 G. Srinivas, J. W. Burress, J. Ford and T. Yildirim, *J. Mater. Chem.*, 2011, **21**, 11323–11329.
14 H. L. Wang, Y. Yang, Y. Y. Liang, L. F. Cui, H. S. Casalongue, Y. G. Li, G. S. Hong, Y. Cui and H. J. Dai, *Angew. Chem., Int. Ed.*, 2011, **50**, 7364–7368.
15 J. Chen, H. Bi, S. R. Sun, Y. F. Tang, W. Zhao, T. Q. Lin, D. Y. Wan, F. Q. Huang, X. D. Zhou, X. M. Xie and M. H. Jiang, *ACS Appl. Mater. Interfaces*, 2013, **5**, 1408–1413.
16 A. Aijaz, A. Karkamkar, Y. J. Choi, N. Tsumori, E. Ronnebro, T. Autrey, H. Shioyama and Q. Xu, *J. Am. Chem. Soc.*, 2012, **134**, 13926–13929.
17 R. Fuhrer, I. K. Herrmann, E. K. Athanassiou, R. N. Grass and W. J. Stark, *Langmuir*, 2011, **27**, 1924–1929.
18 L. Yang, W. Luo and G. Z. Cheng, *ACS Appl. Mater. Interfaces*, 2013, **5**, 8231–8240.
19 D. Ciuculescu, F. Dumestre, M. Comesana-Hermo, B. Chaudret, M. Spasova, M. Farle and C. Amiens, *Chem. Mater.*, 2009, **21**, 3987–3995.
20 C. B. Rong, N. Poudyal, G. S. Chaubey, V. Nandwana, Y. Liu, Y. Q. Wu, M. J. Kramer, M. E. Kozlov, R. H. Baughman and J. P. Liu, *Appl. Phys. Lett.*, 2008, **103**, 07E131.
21 M. Seredych, O. Mabayoje and T. Bandosz, *Langmuir*, 2012, **28**, 1337–1346.
22 M. Seredych, O. Mabayoje and T. J. Bandosz, *J. Phys. Chem. C*, 2012, **116**, 2527–2535.
23 M. J. Allen, V. C. Tung and R. B. Kaner, *Chem. Rev.*, 2010, **110**, 132–145.
24 D. J. Xue, S. Xin, Y. Yan, K. C. Jiang, Y. X. Yin, Y. G. Guo and L. J. Wan, *J. Am. Chem. Soc.*, 2012, **134**, 2512–2515.
25 S. Schrittwieser, F. Ludwig, J. Dieckhoff, K. Soulantica, G. Viau, L. M. Lacroix, S. M. Lentijo, R. Boubekri, J. Maynadié, A. Huetten, H. Brueckl and J. Schotter, *ACS Nano*, 2012, **6**, 791–801.
26 C. F. Zhang, X. Peng, Z. P. Guo, C. B. Cai, Z. X. Chen, D. Wexler, S. Li and H. K. Liu, *Carbon*, 2012, **50**, 1897–1903.
27 S. Park, J. An, R. D. Piner, I. Jung, D. X. Yang, A. Velamakanni, S. T. Nguyen and R. S. Ruoff, *Chem. Mater.*, 2008, **20**, 6592–6594.
28 C. K. Chan, H. Peng, G. Liu, K. McIlwrath, X. F. Zhang, R. A. Huggins and Y. Cui, *Nat. Nanotechnol.*, 2008, **3**, 31–35.
29 T. G. Devi and M. P. Kannan, *Energy Fuels*, 2007, **21**, 596–601.
30 Y. J. Yao, C. Xu, J. C. Qin, F. Y. Wei, M. N. Rao and S. B. Wang, *Ind. Eng. Chem. Res.*, 2013, **52**, 17341–17350.
31 Y. Yao, S. Miao, S. Yu, L. P. Ma, H. Sun and S. Wang, *J. Colloid Interface Sci.*, 2012, **379**, 20–26.

32 H. Wang, L. Cui, Y. Yang, H. S. Casalongue, J. T. Robinson, Y. Y. Liang, Y. Cui and H. Dai, *J. Am. Chem. Soc.*, 2010, **132**, 13978–13980.
33 X. C. Dong, H. Xu, X. W. Wang, Y. X. Huang, M. B. Chan-Park, H. Zhang, L. H. Wang, W. Huang and P. Chen, *ACS Nano*, 2012, **6**, 3206–3213.
34 Z. Chen, W. Ren, L. Gao, B. Liu, S. Pei and H. M. Cheng, *Nat. Mater.*, 2011, **10**, 424–428.
35 L. Y. Zhao, R. He, K. T. Rim, T. Schiros, K. S. Kim, H. Zhou, C. Gutiérrez, S. P. Chockalingam, C. J. Arguello, L. Pálová, D. Nordlund, M. S. Hybertsen, D. R. Reichman, T. F. Heinz, P. Kim, A. Pinczuk, G. W. Flynn and A. N. Pasupathy, *Science*, 2011, **333**, 999–1003.
36 I. Mona, M. G. Cécile, A. Kahina, B. Ekrame, L. Lise-Marie, Z. Lacroix, W. F. Bénédicte, L. Sébastien, D. Philippe, P. Jean-Yves and V. Guillaume, *J. Phys. Chem. C*, 2013, **117**, 15808–15816.
37 T. Maurer, F. Zighem, F. Ott, G. Chaboussant, G. André, Y. Soumare, J. Y. Piquemal, G. Viau and C. Gatel, *Phys. Rev. B: Condens. Matter Mater. Phys.*, 2009, **80**, 064427.
38 L. Tan, L. Pan, C. Cao, B. Wang and L. Li, *J. Power Sources*, 2014, **253**, 193–200.
39 C. G. Tan and R. N. Grass, *Chem. Commun.*, 2008, 4297–4299.
40 W. S. Seo, J. H. Lee, X. Sun, Y. Suzuki, D. Mann, Z. Liu, M. Terashima, P. C. Yang, M. V. McConnell, D. G. Nishimura and H. J. Dai, *Nat. Mater.*, 2006, **5**, 971–976.
41 K. A. Atmane, F. Zighem, Y. Soumare, M. Ibrahim, R. Boubekri, T. Maurer, J. Margueritat, J. Y. Piquemal, F. Ott, G. Chaboussant, F. Schoenstein, N. Jouini and G. Viau, *J. Solid State Chem.*, 2013, **197**, 297–301.
42 P. R. Shukla, S. Wang, H. Sun, H. M. Ang and M. Tadé, *Appl. Catal., B*, 2010, **100**, 529–534.
43 Ö. Metin, V. Mazumder, S. Özkar and S. H. Sun, *J. Am. Chem. Soc.*, 2010, **132**, 1468–1469.
44 J. Mahmood, S. M. Jung, S. J. Kim, J. Park, J. W. Yoo and J. B. Baek, *Chem. Mater.*, 2015, **17**, 4860–4864.
45 R. Li, Y. Yang, R. Li and Q. W. Chen, *ACS Appl. Mater. Interfaces*, 2015, **7**, 6019–6024.
46 W. H. Chong, L. K. Chin, R. L. S. Tan, H. Wang, A. Q. Liu and H. Y. Chen, *Angew. Chem., Int. Ed.*, 2013, **52**, 8570–8573.
47 S. L. Yang, C. Y. Cao, Y. B. Sun, P. P. Huang, F. F. Wei and W. G. Song, *Angew. Chem., Int. Ed.*, 2015, **54**, 2661–2664.
48 Q. Wan, T. H. Wang and J. C. Zhao, *Appl. Phys. Lett.*, 2005, **87**, 08310.
49 B. J. Li, H. Q. Cao and G. Yin, *J. Mater. Chem.*, 2011, **21**, 13765–13768.